LANGMUIR

pubs.acs.org/Langmuir Article

Nanobubble-Induced Aggregation of Ultrafine Particles: A Molecular Dynamics Study

Eric Bird and Zhi Liang*

Cite This: *Langmuir* 2023, 39, 9744−9756 Read Online

ACCESS | Metrics & More | Article Recommendations

ABSTRACT: Nanobubble-induced aggregation (NBIA) of fine and ultrafine particles in liquid is a promising method for enhancing floatation rates in mineral processing, cleaning contaminants from water, and reviving marine ecosystems. Although the current experimental techniques can measure the nanobubble capillary force between two surfaces with controlled approach speed, they are not capable of imaging NBIA dynamics of fine/ultrafine particles by real-time observation with nanoscale spatial resolution. In this work, we use molecular dynamics (MD) simulations to study dynamics of NBIA of Ag particles in a Lennard−Jones fluid system. The molecular-level modeling allows us to study microscopic details of NBIA dynamics that are inaccessible by current experimental means. Using MD simulations, we investigated the effects of NB size, surface wettability, surface roughness, and contact line pinning on NBIA dynamics. Our modeling results show that both concave NB bridges between two hydrophobic surfaces and convex NB bridges between two hydrophilic surfaces can result in an attractive nanobubble capillary force (NBCF) that causes the aggregation of Ag particles in liquids. The equilibrium separation between two fully aggregated particles can be well predicted by the improved capillary force model. We also observe that the change of contact angle after the contact line pinning occurs at the sharp edge of a particle, which slows the aggregation process. Our thermodynamics analysis shows that there is a critical contact angle below which the merged surface NBs will detach from the surface instead of causing aggregation. The prediction of the critical contact angle is corroborated by our MD simulation results.

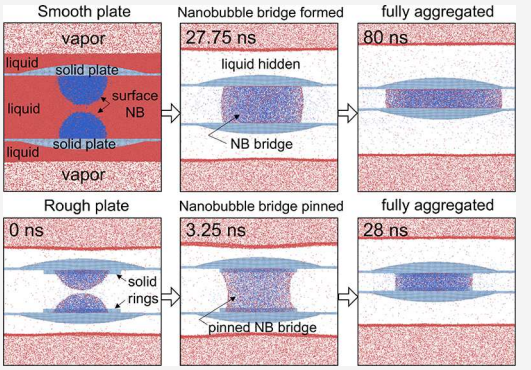

1. INTRODUCTION

The lifetime of ordinary macrobubbles in liquids is usually on the order of seconds because macrobubbles rise rapidly to liquid surfaces due to the buoyancy force and then burst. As the bubble size reduces, the terminal rise velocity of a spherical bubble quickly decreases. When the bubble size is less than 1 μm, the buoyancy effect on bubbles is insignificant compared to Brownian motion. As a result, nanobubbles (NBs), whose diameter is less than 1 μm, can persist in liquid for hours or even days.[1]

Because of their longevity in liquids, NBs have much higher possibility to attach to particle surfaces than ordinary macrobubbles.[2] When two fine/ultrafine particles in liquids approach, the NBs on the adjoining surfaces can coalesce and form a gas bridge, which results in an attractive capillary force. The NB capillary force (NBCF) between fine/ultrafine particles leads to the aggregation of these particles in liquids. With the assistance of NBs, the aggregated particles have a larger apparent particle size. Hence, they can be more easily captured by macrobubbles, which will provide enough buoyancy forces to elevate particles to the liquid surface. A number of recent experimental studies have reported a significant increase of the flotation rate of fine (<37 μm) and ultrafine fine (<10 μm) mineral particles in the presence of NBs.[2−4] With a similar mechanism, NBs can also be used in many other industrial applications such as wastewater treatment, detergent-free cleaning, and deinking to remove fats, oil, grease, and suspended solids from wastewater, clothes, and recycled paper.[5−7] The key process in all these applications is the nanobubble-induced aggregation (NBIA) of fine/ultrafine particles in liquid. Therefore, a fundamental understanding of the NBIA process is essential for more efficient use of NBs in various industrial applications.

Although there have been intensive efforts to study the dynamics of NBs and the NBCF between two surfaces using optical methods,[8,9] atomic force microscopy (AFM),[10,11] in situ transmission electron microscope (TEM),[12] and other experimental approaches,[11,13] experimental study of the NBIA

Received: March 23, 2023
Revised: May 17, 2023
Published: July 3, 2023

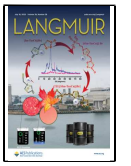

https://doi.org/10.1021/acs.langmuir.3c00787
Langmuir 2023, 39, 9744−9756

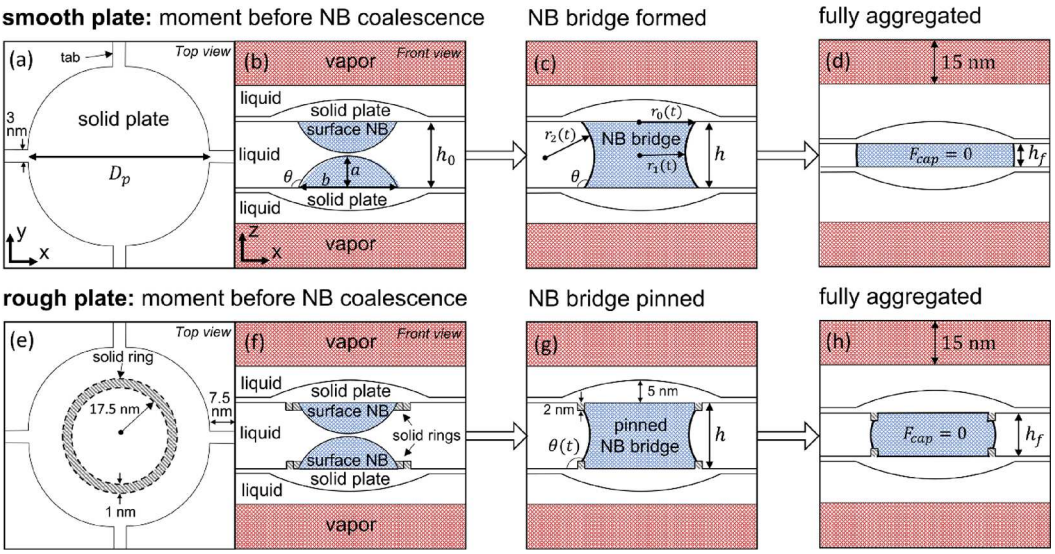

Figure 1. Schematic of model system showing (a) the top view of the solid plate, (b) the front view of surface NBs attached to solid plates surrounded by liquid and two vapor regions, (c) the NB bridge with geometric parameters, and (d) geometry of the NB bridge between fully aggregated plates. Panels e–h are the same as a–d except with rough solid surfaces.

process is still very challenging as it requires measurement of the NBCF and the geometry of NB capillary bridge between aggregating particles in nanoscale time and spatial resolution. The fast growth in computing power in the past decades creates an opportunity to use molecular dynamics (MD) simulations to study the NBIA process. The molecular-level modeling allows us to study microscopic details of the NBIA process that are inaccessible by experimental means. Moreover, such microscopic understanding and predictions are not hindered by many assumptions and approximations such as velocity slip and contact angle boundary conditions used in continuum and theoretical modeling.

In our previous work,[14] we have successfully used MD simulations to measure both the geometry of the NB gas bridge between two stationary solid surfaces and the resulting NBCF and explicitly verified the relationship between the NBCF and the NB bridge geometry that is predicted by the capillary force theoretical model.[14−16] In this work, we will dive deeper into the dynamic NBIA process by releasing the constraint on the positions of two solid surfaces that are connected by a single NB bridge in MD simulations. Specifically, we will carry out MD simulations to investigate the effects of NB size, surface wettability, surface roughness, and contact line pinning on the aggregation speed, final state of the particle agglomeration, and whether the particle aggregation will occur. To provide a fundamental understanding of the modeling NBIA processes, we will utilize the capillary force model and thermodynamic models to analyze the MD simulation results in this work.

The remainder of the paper is organized into the following sections: Section 2 introduces the capillary force model that will be used for analysis of the model NBIA processes. Section 3 describes the MD model used for the simulation of NBIA of Ag particles in liquids. Section 4 presents the MD simulation results on how the NBIA processes are affected by the size of surface NBs, wettability of particle surfaces, and surface roughness. We will use the MD simulation results to test the accuracy of the capillary force model in the prediction of the equilibrium separation between two fully aggregated particles. In Section 5, we combine MD simulation results and the thermodynamics analysis to investigate the critical contact angle below which the merged surface NBs will detach from the surfaces instead of causing aggregation. Last, we close with conclusions.

2. IMPROVED CAPILLARY FORCE MODEL

2.1. Dependence of the NBCF on NB Bridge Geometry. The driving force for the nanobubble-induced aggregation (NBIA) of particles in liquids is the nanobubble capillary force (NBCF) acting on solid surfaces. Therefore, the most important issue for understanding the NBIA dynamics is to develop a theoretical model that is capable of predicting the variation of the NBCF in the NBIA process. We start with the simple capillary force model[14−16] that provides the relationship between the NBCF and the geometry of NB bridge between two adjoining surfaces. For an NB gas bridge between two parallel surfaces as shown in Figure 1, the simple capillary force model predicts that the resulting NBCF (F_{cap}) has two components:[14]

$$F_{cap} = -2\pi r_0 \gamma \sin\theta + \pi r_0^2 \Delta P, \quad (1)$$

where the first component is the surface tension force acting at the three-phase contact line and the second component is the pressure force due to the pressure difference (ΔP) between the gas inside the NB bridge and the surrounding liquid. In eq 1, r_0 is the contact radius of the NB gas bridge on the solid surface as shown in Figure 1c, and γ and θ are the liquid−gas surface tension and liquid-side contact angle, respectively. The sign convention in the capillary force model is that negative force is attractive and positive force is repulsive.

The gas inside the NB bridge is a mixture of saturated vapor of the surrounding liquid and other gases that fill the NB bridge. Accordingly, ΔP in eq 1 is given by

$$\Delta P = P_{sat} + P_g - P_L, \quad (2)$$

where P_g is the pressure of gas (excluding saturated vapor) in the NB bridge, P_{sat} is the saturated vapor pressure that has a fixed value at a given temperature, and P_L is the surrounding liquid pressure. During the NBIA process, P_L can be usually

https://doi.org/10.1021/acs.langmuir.3c00787
Langmuir 2023, 39, 9744−9756

considered as a constant, but P_g will vary with the volume of the NB gas bridge as particle surfaces approach. Assuming that the gas inside the NB bridge is an ideal gas, we have

$$P_g = N_g k_B T/V, \tag{3}$$

where T and V are the temperature and volume of the NB gas bridge, respectively, N_g is the number of gas molecules in the bridge, and k_B is the Boltzmann constant. The main difference between the simple capillary force model and the improved capillary force model developed in our previous work[14] is that the improved model replaces the constant volume assumption of the gas bridge in the simple model with eq 3. The improved capillary force model instead assumes a constant number of gas molecules within the NB gas bridge. Therefore, to determine the gas pressure in eq 3, we calculate the bridge volume over time as a function of bridge geometry. Using the toroidal approximation of the NB gas bridge,[15] the volume V and the liquid−gas interface area A of the gas bridge are given by[14]

$$V = 2\pi\left[(r_1 + r_2)r_2^2\left(\frac{\pi}{2} - \theta + \frac{1}{2}\sin 2\theta\right) - r_2(r_1 + r_2)^2\cos\theta - r_2^3\left(\cos\theta - \frac{\cos^3\theta}{3}\right)\right] \tag{4}$$

and

$$A = 4\pi[(r_1 + r_2)r_2(\theta - \pi/2) + r_2^2\cos\theta], \tag{5}$$

where r_1 and r_2 are the principal radii of the NB gas bridge as shown in Figure 1c. In eqs 4 and 5, r_1 is always positive, and r_2 is positive for concave gas bridges and negative for convex gas bridges. In our previous work,[14] we fixed the separation (h) between two surfaces to allow the NB bridge to reach equilibrium with the surrounding liquid before we measured the NB geometry and the resulting F_{cap}. In this case, the pressure difference between the gas inside the NB bridge and the surrounding liquid is equal to the Laplace pressure:

$$\Delta P = \gamma\left(\frac{1}{r_1} - \frac{1}{r_2}\right). \tag{6}$$

Therefore, we directly used the Laplace pressure, i.e., eq 6, in our previous work[14] to calculate the pressure force component of F_{cap}. In this work, however, we release the constraints on surface positions of the solid particles to study the dynamic NBIA process. As the two surfaces are pulled by the NBCF to approach each other, the NB bridge between them is forced to expand in the lateral direction, which implies that the Laplace pressure does not balance out the pressure difference between the gas and the surrounding liquid. Therefore, we rely on eq 2 rather than eq 6 to determine ΔP in this work.

One of the advantages of MD simulations is that the geometry of the evolving NB bridge between two surfaces can be directly measured at nanoscale spatial and time resolution. In this work, we will use MD simulations to measure the geometric parameters r_0, r_1, r_2, and θ of an NB bridge during the model NBIA process and substitute these parameters into eqs 1 through 4 to find F_{cap} at different separations between two solid surfaces.

2.2. Equilibrium Separation between Two Surfaces. Upon the coalescence of two surface NBs, an NB gas bridge is formed between two surfaces. If the surfaces are hydrophobic, the NB bridge between them is concave such as that shown in Figure 1c. For a concave NB bridge, the NBCF remains attractive as the two surfaces get closer.[14,17−19] As a result, the concave NB bridge will draw the two particles toward each other until the solid surfaces are in contact, which results in a repulsion force that balances the attractive NBCF. If the solid surfaces are hydrophilic, the NB bridge between them becomes convex. For a convex NB bridge, the NBCF exhibits a transition from attractive to repulsive as the two surfaces approach each other.[14,17−19] This indicates that there is an equilibrium separation between two hydrophilic surfaces at which the NBCF equals to zero. At the equilibrium separation, the NB bridge and the distance between two solid surfaces will be stable.

To obtain the theoretical prediction of the equilibrium separation (h_f) that makes $F_{cap} = 0$, we apply the improved capillary force model described in Section 2.1. Eqs 1 through 4 show that F_{cap} depends on seven parameters, i.e., r_0, r_1, r_2, γ, θ, T, and N_g. For a given NBIA process, the surface tension (γ) and temperature (T) can be considered as constant. In addition, we assume that the contact angle (θ) and the number of gas molecules (N_g) within the gas bridge will not change in the NBIA process. We will verify this assumption in our MD simulations. Accordingly, F_{cap} only depends on the three geometric parameters, r_0, r_1, and r_2, which will vary with the separation (h) between solid surfaces in the NBIA process. To find the final equilibrium separation (h_f) that makes $F_{cap} = 0$, therefore, we need three additional equations for the dependence of r_0, r_1, and r_2 on h. We showed in our previous work[14] that the three equations include two trigonometric relations:

$$r_2 = -h/(2\cos\theta) \tag{7}$$

and

$$r_0 = r_1 + r_2(1 - \sin\theta). \tag{8}$$

The third equation is obtained by making eq 2 equal to eq 6:

$$P_{sat} + N_g k_B T/V - P_L = \gamma\left(\frac{1}{r_1} - \frac{1}{r_2}\right), \tag{9}$$

where the NB bridge volume (V) is given by eq 4. As we discussed in Section 2.1, the Laplace pressure (i.e., eq 6) is not equal to eq 2 in the NBIA process. At the equilibrium separation, however, the NB bridge between two surfaces will become stable, which means that the Laplace pressure balances the pressure difference between the gas inside the NB bridge and the surrounding liquid. Therefore, it is valid to use eq 9 to predict the final equilibrium separation.

Using the three coupled equations (i.e., eqs 7−9), we can find r_0, r_1, and r_2 as a function of h numerically. Substituting these results into eq 1, we find the dependence of F_{cap} on h for an NB bridge with given θ, T, and N_g. From the F_{cap} vs h curve, we can readily obtain the equilibrium separation (h_f) that makes $F_{cap} = 0$. The theoretical model described in this section is the improved capillary force model developed in our previous work[14] for the study of NBCF between two stationary plates. The improved capillary force model shows that for an NB bridge between two parallel solid surfaces in a given liquid, the F_{cap} vs h relation only depends on three parameters, i.e., θ, T, and N_g. Accordingly, the equilibrium separation (h_f) is determined by θ, T, and N_g. In this work, we will verify the theoretical prediction of h_f by comparing to MD simulation results.

https://doi.org/10.1021/acs.langmuir.3c00787
Langmuir 2023, 39, 9744−9756

3. MD SIMULATION OF THE NBIA PROCESS

3.1. The MD Model System. The MD model system is meant to simulate the coalescence of surface nanobubbles (NBs) and the subsequent aggregation of solid particles in liquids due to the nanobubble capillary force (NBCF). As shown in Figure 1, the model system consists of two surface neon (Ne) NBs attached to solid silver (Ag) plates submerged in saturated liquid argon (Ar). A system temperature of 85 K is chosen because the properties of saturated model liquid Ar at T = 85 K have been studied in our previous work,[20−24] and we can directly use these fluid properties in this work. Two 15 nm tall Ar vapor regions are positioned above and below the liquid bath to accommodate the liquid volume change during the model nanobubble-induced aggregation (NBIA) process and maintain the liquid pressure P_L around P_{sat} of the model Ar at the given temperature.[14,25,26] Periodic boundary conditions (PBCs) are applied in all three directions. In our previous work,[14] we used the same model fluid system to study the NBCF between two stationary Au plates. In this study, we switch to Ag plates because Ag is much lighter than Au, thus reducing the total aggregation time and saving the computational cost.

Each solid Ag plate in the model system is a composite of three (for smooth surfaces) or four (for rough surfaces) parts. The first part is a circular disk formed by five FCC (001)-oriented Ag atomic layers. The diameter (D_p) of the Ag circular disk ranges from 50 to 60 nm depending on the initial size of surface NBs. The second part contains four Ag tabs attached to the circular disk in the $\pm x$ and $\pm y$ directions, respectively. As shown in Figure 1, each of the four tabs has a length of 7.5 nm, a width of 3 nm, and the same thickness as the circular disk. The Ag tabs interconnect across the periodic boundaries, which ensure that the inner surfaces of the two Ag plates remain parallel to each other during the aggregation process. The third part of each Ag plate is a spherical cap at the outside surface of the plate as shown in Figure 1. The diameter of the base of the cap is the same as that of the circular disk, and the height of the spherical cap is 4 nm. The spherical cap is a reinforcement part to reduce the deformation of the Ag plate induced by the NBCF. In the case of rough solid surfaces, a solid Ag ring (i.e., the fourth part of the plate) with an inner radius of 17.5 nm, width of 1 nm, and thickness of 2 nm will be added to the inside surface of each plate as shown in Figure 1e−h. In all cases, the corner gaps of the Ag plates allow liquid flow through them during the aggregation process.

The embedded-atom-method (EAM) potential[27] is used to model the interatomic interactions in Ag plates. All fluid−fluid and fluid−solid interactions are described by a modified Lennard−Jones (LJ) potential:

$$E_p(r) = 4\varepsilon[(\sigma/r)^{12} - c(\sigma/r)^6], \quad (10)$$

where c is a tunable parameter mainly used to adjust the contact angle of the model fluid on solid surfaces. Our goal is not to study the NBIA aggregation of Ag particles in liquid Ar specifically but to make general observations about how the NB size, contact angle, and surface roughness affect the NBIA aggregation process. In eq 10, the coefficient c is fixed at 1.0 for all fluid−fluid interactions and is tuned to lower values for Ar−Ag interactions to adjust the contact angle. For Ne−Ag interactions, the c value in eq 10 (i.e., the attraction part of the potential) is set to zero to minimize the diffusion of Ne gas molecules through the three-phase contact line.[28,29] The potential parameter σ for Ar−Ag and Ne−Ag interactions is determined from the Lorentz-Berthelot mixing rule[30] with σ_{Ag} taken from the universal force field (UFF).[31] Table 1 summarizes the potential parameters ε and σ used in the simulation. The cutoff distance for all LJ interactions is 10.9 Å. The velocity Verlet algorithm[32] is used with a timestep of 5 fs for all MD simulations. The long-range corrections to the pressure and potential energy are not considered in our MD model as the model system is highly inhomogeneous and multiphased. All MD simulations are performed using the LAMMPS simulation package.[33]

Table 1. LJ Parameters Used in the MD Simulations

	Ar−Ar[30]	Ne−Ne[30]	Ar−Ne[25]	Ar−Ag	Ne−Ag
ε (meV)	10.3	4.05	4.05	10.3	4.05
σ (Å)	3.41	2.72	3.41	3.12	2.76

In our previous work,[25] we have used the same potential model to study the coalescence dynamics of bulk Ne NBs in liquid Ar and found that the liquid−gas surface tension γ = 0.0107 N/m and saturated liquid Ar density ρ_{sat} = 1360 kg/m^3 at T = 85 K. We will use γ and ρ_{sat} obtained from our previous work to analyze the simulation results in this work.

3.2. Variation of Contact Angles with Surface Wettability. *3.2.1. Contact Angles of Surface Droplets.* In this work, we tune the surface wettability by varying the c value in eq 10. Determination of the contact angle at different c values is important for the initialization of surface NBs in the MD simulation of NBIA processes and analysis of the simulation results. Therefore, we first carry out separate MD simulations to determine the contact angle of the model liquid Ar on Ag surfaces.

As shown in Figure 2a−d, we place a liquid Ar droplet on a Ag plate. The simulation box has a length of 25 nm in the vertical direction and a cross-section area of 35 × 35 nm. The Ag plate is a composite of a circular disk and a spherical cap. The diameters of the circular disk and the cap base are both 25 nm. The height of the circular disk and the cap is 5 FCC (001)-oriented atomic layers and 4 nm, respectively. For each given c value, we adjust the number of Ar atoms in the model system so that the diameter of the equilibrium liquid Ar droplet is around 15 nm. A constant number of atoms, constant volume, and constant temperature (NVT) simulation is first carried out for 500 ps to equilibrate the model system at a temperature of 85 K using a Nose−Hoover thermostat.[34] Afterward, we turn off the thermostat in the model fluid and only apply the thermostat in the solid plate for another 500 ps to let the three-phase system reach thermal equilibrium. After equilibration, the contact angle θ of the model liquid Ar on Ag plate is calculated by measuring the height (a) and contact diameter (b) of the droplet in snapshots and plugging them into eq 11:

$$\theta = 2\tan^{-1}(2a/b). \quad (11)$$

As shown in Figure 2a−d, we can gradually tune the Ag surface from hydrophobic to hydrophilic by increasing the c value from 0.45 to 0.65.

Our goal is to use the calculated contact angle to initialize the surface NB on the same solid surface and analyze the model NBIA process. However, it was observed in some experiments[35] that the liquid-side contact angle of surface NBs is higher than that measured from surface liquid droplets. The

https://doi.org/10.1021/acs.langmuir.3c00787
Langmuir 2023, 39, 9744−9756

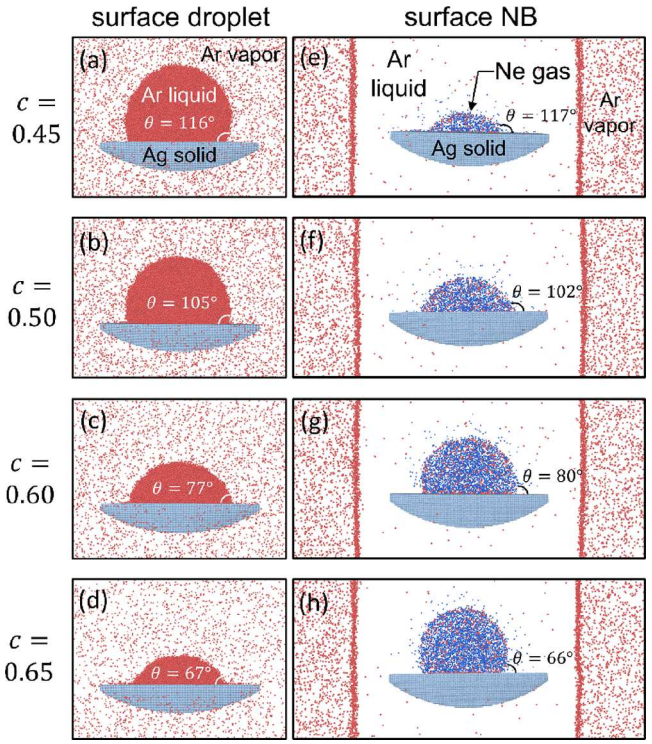

Figure 2. Snapshots of equilibrium (a–d) surface droplets and (e–h) surface NBs and their contact angles. Red, blue, and gray dots represent Ar, Ne, and Ag atoms, respectively. The liquid Ar atoms are hidden in panels e–h to clearly show the surface NBs.

discrepancy is attributed to the diffusion of gas molecule through the three-phase contact line of surface NBs, which results in a gas enrichment layer at the solid–liquid interface, making the surface more hydrophobic.[29] To eliminate the complexity induced by the possible gas enrichment layer, we set the attraction part of the Ne–Ag potential to zero to minimize the effect of the gas enrichment layer on contact angles. To verify that the liquid-side contact angle of surface NBs is equal to that of surface droplets in our model, we further carry out separate simulations of isolated surface NBs in Section 3.2.2.

3.2.2. Contact Angles of Surface NBs. As shown in Figure 2e–h, we place a solid Ag plate the same as that in Figure 2a–d in a simulation box with dimensions of 55 × 35 × 25 nm. The solid plate is immersed in a liquid Ar flanked by two 10 nm thick vapor Ar regions in which vapor Ar is in equilibrium with the liquid Ar at T = 85 K. An NVT simulation is carried out for 1.5 ns using a Nose–Hoover thermostat.[34] After equilibration, a spherical cap shaped surface NB region is defined on the solid surface, and all Ar atoms inside are deleted. The surface NB region is defined by its diameter D_{NB} and contact angle θ. We use the θ obtained from the above surface droplet simulation as a guess of the contact angle for the surface NB and set D_{NB} = 15 nm in all cases. The number of Ne gas atoms N_{Ne} inside the surface NB is calculated by combining the ideal gas and Young–Laplace equations:

$$N_{Ne} = \left(\frac{4\gamma}{D_{NB}}\right)\frac{V_{NB}}{k_B T}, \quad (12)$$

where V_{NB} is the volume of the spherical cap shaped NB region. Ne atoms are inserted randomly into the spherical cap region. Subsequently, the NVT simulation is performed for another 250 ps to let the model system reach equilibrium at T = 85 K. We check the Ar and Ne potential energies over time to ensure that a plateau is reached to confirm that the system is in equilibrium. To clearly show the surface NBs after equilibration, we hide all liquid Ar atoms in snapshots shown in Figure 2e–h. An Ar atom is defined as a liquid atom if its potential energy is lower than half of that in a saturated liquid Ar at T = 85 K. We have successfully used this method to clearly show the geometry of NB gas bridges in our previous work.[14,25,26] Using the height and contact diameter of the surface NBs measured from the snapshots in Figure 2e–h, we calculate the gas-side contact angle from eq 11. The supplement of the gas-side contact angle is the liquid-side contact angle of surface NBs.

As shown in Figure 2, the liquid-side contact angles between the surface NBs and surface droplets agree very well for each c value, indicating the negligible effects of the gas enrichment layer on the contact angle of surface NBs in our model. This is also apparent by inspecting Figure 2e–h, where almost no Ne atoms are attached to the solid surface. Therefore, the NB contact angles are solely influenced by the Ar–Ag interaction strength in our model system. This is advantageous for our study because we can control the NB contact angles by modifying the Ar–Ag interaction strength without the interference of gas layers at the solid surface. We will use the contact angles obtained in this section to set up initial surface NBs in the MD simulation of NBIA processes.

3.3. Procedures for NBIA Simulations. *3.3.1. Initialization of the Model System for NBIA Simulations.* To initialize the model system for NBIA simulations, we first place two solid Ag plates in the simulation box as shown in Figure 1b or f and fill the liquid region with model Ar atoms at a density of ρ_{sat}. An NVT simulation with a Nose–Hoover thermostat is carried out for 1.5 ns to equilibrate the model system at a temperature of 85 K. After equilibration, we use a similar method as described in Section 3.2.2 to generate a surface NB on each of the two solid Ag plates.

We have determined the contact angle of surface NBs at different c values in Section 3.2. From the known contact angle and diameter of surface NB, we can readily predict the height of the surface NBs with precision. With this prediction, we choose a proper initial separation (h_0) between the two plates such that the separation between two equilibrated surface NBs is 2–3 nm. To make the two adjoining surface NBs coalesce,

Table 2. Simulation Parameters and Equilibrium Separation for NBIA of Hydrophilic Surfaces with an Initial Contact Angle of $\theta \approx 80°$

simulation case	simulation box size (nm)	D_p (nm)	D_{NB} (nm)	h_0 (nm)	h_f (nm)	$h_{f,theo}$ (nm)	N_{Ne}
1	75 × 75 × 80	60	25	30.3 ± 0.2	9.4 ± 0.2	9.6	16,748
2	75 × 75 × 67.5	60	—	5.0 ± 0.2	9.4 ± 0.2	9.6	16,748
3	70 × 70 × 75	55	20	24.5 ± 0.2	7.9 ± 0.2	7.8	10,718
4	75 × 75 × 75	60	15/25	25.0 ± 0.2	8.4 ± 0.2	8.4	11,389

https://doi.org/10.1021/acs.langmuir.3c00787
Langmuir 2023, 39, 9744–9756

Table 3. Simulation Parameters and Equilibrium Separation for NBIA of Hydrophobic Surfaces with an Initial Contact Angle of $\theta \approx 102°$

simulation case	simulation box size (nm)	D_p (nm)	D_{NB} (nm)	h_0 (nm)	h_f (nm)	N_{Ne}
5	75 × 75 × 70	60	25	20.3 ± 0.2	5.0 ± 0.2	9162
6	65 × 65 × 65	50	20	15.8 ± 0.2	4.1 ± 0.2	5864
7	75 × 75 × 65	60	15/25	16.2 ± 0.2	3.6 ± 0.2	6230

Table 4. Simulation Parameters and Equilibrium Separation for NBIA of Rough Surfaces

simulation case	simulation box size (nm)	θ (°)	D_p (nm)	D_{NB} (nm)	h_0 (nm)	h_f (nm)	N_{Ne}
8	75 × 75 × 80	80 ± 3	60	25	30.3 ± 0.2	13.4 ± 0.2	16,748
9	75 × 75 × 70	102 ± 3	60	25	20.5 ± 0.2	8.6 ± 0.2	9162

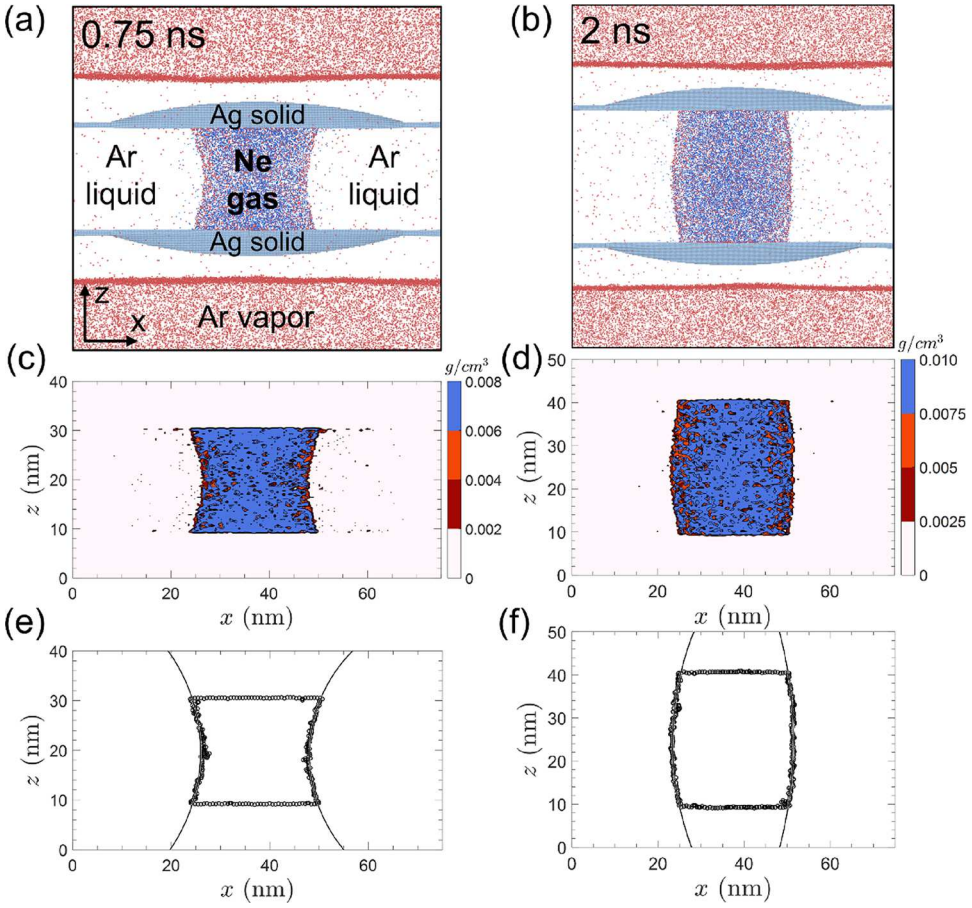

Figure 3. Snapshots (a, b), isodensity contours (c, d), and geometric fitting (e, f) of the (a) concave NB bridge and (b) convex NB bridge.

we set the number of Ne gas atoms (N_{Ne}) in each surface NB slightly greater than that predicted from eq 12. After Ne atoms are inserted into the surface NB regions, we first carry out an NVT simulation at T = 85 K for 250 ps to equilibrate the system containing surface NBs. For each case of MD simulations, we carefully select N_{Ne} so that the NBs will not coalesce before they reach equilibrium. Within the 250 ps equilibration period, the surface NBs expand a small amount and reach equilibrium, but no coalescence of surface NBs occurs. Afterward, we turn off the thermostat on fluids and equilibrate the model system for another 500 ps. Within 500 ps, the Brownian motions of Ag plates and fluctuations of liquid−gas interfaces of surface NBs lead to the coalescence of surface NBs. We start the analysis of the NBIA process upon the coalescence of surface NBs.

In Tables 2−4, we summarize the simulation parameters, including the simulation box size, diameter of Ag plates (D_p), diameter of NBs (D_{NB}), contact angle (θ), initial separation between two plates (h_0), and total number of Ne atoms (N_{Ne}) in the two surface NBs, that are selected for each simulation case in this work.

3.3.2. Analysis of NBIA Processes. Upon coalescence of the two NBs, a capillary gas bridge is formed between two solid surfaces. Because of the capillary force produced by the NB bridge, the plates will begin to move. To understand the NBIA process, we will monitor the time variation of the separation (h) between two plates, F_{cap}, and the number of Ne gas atoms (N_{Ne}) within the NB bridge until the separation (h) fluctuates around a constant and the NB gas bridge becomes stable. At this point, the equilibrium separation distance h_f is reached where the capillary force F_{cap} = 0.

https://doi.org/10.1021/acs.langmuir.3c00787
Langmuir 2023, 39, 9744−9756

Whereas the separation (h) between two plates can be readily obtained from positions of Ag atoms in MD simulations, determination of F_{cap} requires the measurement of the geometric parameters θ, r_0, r_1, and r_2 of the NB bridge over time in MD simulations. To determine the transient geometry of NB bridges, we output the position of every atom except the liquid Ar atoms in the model system as we did in Section 3.2.2 every 250 ps. Using the transient atom positions, we generate snapshots of the model system as shown in Figure 3a,b, which clearly demonstrate the transient geometry of the NB bridge between two Ag surfaces. The contact radius r_0 and the principal radius r_1 of the NB bridge can be measured at the plate surface and at the center of the bridge, respectively, by inspection of each snapshot using the molecular visualization program Ovito.[36] The principal radius r_2 and contact angle θ of the NB bridge can be calculated from the measured r_0, r_1, and h using trigonometric relations:[14]

$$r_2 = \frac{h^2 + 4(r_0 - r_1)^2}{8(r_0 - r_1)} \tag{13}$$

and

$$\theta = \cos^{-1}(-h/2r_2). \tag{14}$$

Although it is possible to use the aforementioned method to manually measure the geometric parameters from each snapshot as done in our previous work with NB bridges between two stationary plates,[14] it becomes prohibitive in the study of NBIA processes because the total number of snapshots to be processed in this work exceeds 2000. Therefore, we develop a systematic approach to consistently determine the geometric parameters of any NB bridge from atomic positions.

The visualization approach used to determine the transient geometry of NB bridges is similar to that commonly used in MD droplet studies,[37,38] which involves dividing the system into bins to plot the density profile. We divide the simulation box evenly into 125 × 125 × 125 rectangular bins and calculate the density of Ne in each bin from positions of Ne atoms. Bins with a Ne density greater than half of the bulk Ne density in the center of NB bridge are averaged in the y direction to achieve a 2D density view. Hence, bins in the liquid region where Ne density is almost zero are mostly excluded in the y-direction averaging. Isolines are plotted and filled with different colors for four density ranges as shown in Figure 3c,d. The location of liquid−gas interface is identified where the density of Ne is half of that in the bulk Ne gas within the NB bridge. We find that using a half-density of Ne gas criteria (Figure 3c,d) predicts the same interface location as the half-potential of Ar criteria (Figure 3a,b). Therefore, because of the convenience of the half-density gas criteria, the vertices of the half-density isoline are used to fit circular arcs to the 2D interfaces as shown in Figure 3e,f. Using the combination of the intersurface separation and the fitted arcs at the interface, all geometric parameters, including the contact radius (r_0), principal radii (r_1 and r_2) of the NB bridge, contact angle (θ), and separation (h) between plates, are determined directly from the density analysis of the model fluid. From the location of the liquid−gas interface of the NB bridge, we directly count the number of Ne gas atoms (N_{Ne}) within the NB bridge. Thus, the geometry parameters of the NB bridges and the number of gas atoms inside the NB bridge are systematically calculated every 250 ps for every simulation case to understand the NBIA processes.

4. MODELING RESULTS

4.1. NBIA of Smooth Hydrophilic Surfaces. *4.1.1. Comparison of MD Simulation Results and Theoretical Predictions.* To study the nanobubble-induced aggregation (NBIA) of smooth hydrophilic surfaces, we set c = 0.60 for argon−silver (Ar−Ag) interactions, which results in a liquid-side contact angle $\theta \approx 80°$. A neon (Ne) nanobubble (NB) with an initial diameter of around 25 nm is generated on each of the two smooth Ag surfaces using the method described in Section 3.3.1. The total number of Ne atoms in the two Ne NBs is 16,748. All simulation parameters are summarized as case #1 in Table 2. The coalescence of NBs on adjoining hydrophilic surfaces results in a convex NB bridge that leads to the aggregation of two Ag surfaces as shown in Figures 4 and 5a.

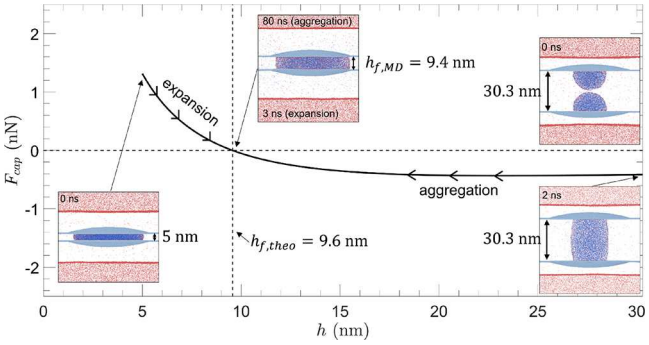

Figure 4. F_{cap} vs h predicted by the improved capillary force model. For a given θ, T, and N_g, eqs 7−9 are used to numerically predict r_0, r_1, and r_2 as a function of h. Equations 2−4 calculate the Laplace pressure ΔP. All parameters are then used in eq 1 to calculate F_{cap} vs h as shown. The top-right and bottom-left snapshots show the starting point of the MD simulation case #1 and case #2, respectively. The bottom-right snapshot shows the NB bridge right after the coalescence of surface NBs. The middle snapshot shows the equilibrium position of two solid plates.

For a model convex NB bridge with N_g = 16,748 gas molecules and θ = 80° at T = 85 K, we first use the improved capillary force model described in Section 2.2 to obtain the theoretical prediction of F_{cap} vs h as shown in Figure 4. Although this prediction may not be accurate during the nonequilibrium NBIA process, it can be used for qualitative understanding of the MD simulation result. Figure 4 predicts that the convex NB bridge will result in a negative (i.e., attractive) F_{cap} at the initial separation (h_0 = 30.3 nm). Under the attractive F_{cap}, the two Ag surfaces will approach each other until the equilibrium separation (h_f) where a transition from attractive F_{cap} to repulsive F_{cap} will occur. From the F_{cap} vs h prediction, therefore, it is reasonable to expect that the distance between the two aggregating hydrophilic surfaces will eventually fluctuate around the equilibrium separation (h_f). As shown in Figure 4, the improved capillary force model predicts h_f = 9.6 nm.

To verify the theoretical prediction, we directly analyze the data obtained from the MD simulation of the NBIA process. It is shown in Figure 5a that under the attractive F_{cap} induced by the convex NB bridge, the two Ag plates approach each other. The motion of Ag plates in the liquid resulted in a drag force

https://doi.org/10.1021/acs.langmuir.3c00787
Langmuir 2023, 39, 9744−9756

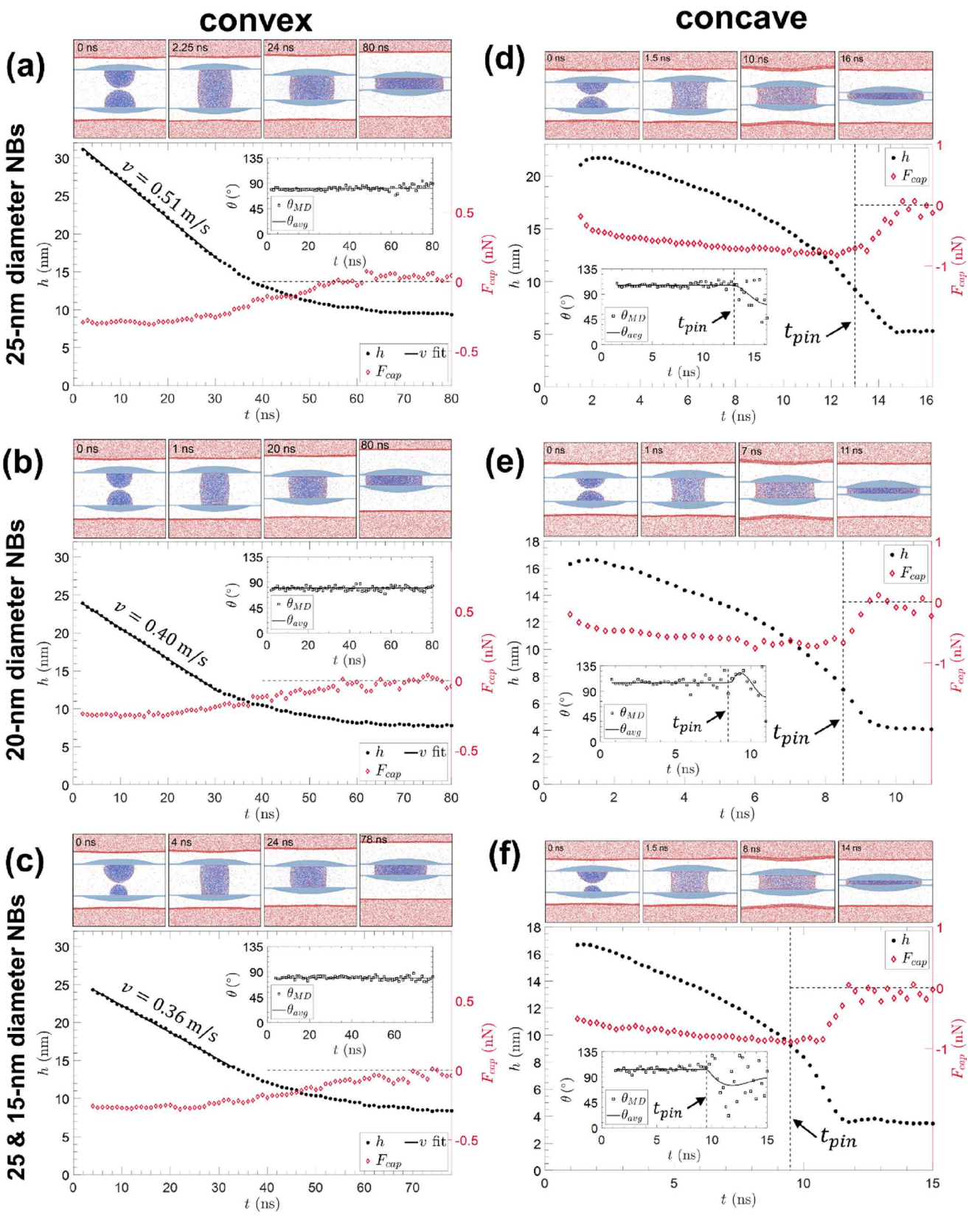

Figure 5. Separation distance, capillary force, and contact angles over time for differently sized concave (a–c) and convex (d–f) NB bridges and their snapshots. The capillary force F_{cap} is calculated in eq 1 using r_0, r_1, r_2, and θ found from MD snapshots. Convex cases (a–c) directly use θ_{MD} to calculate F_{cap}, whereas concave cases (d–f) use θ_{avg} to calculate F_{cap}.

that opposes plates' motion. From the measured h over time shown in Figure 5a, we found that the approaching speed in the initial 30 ns of the aggregation process was essentially a constant around 0.51 m/s, which means that an equilibrium between the attractive F_{cap} and the drag force was established soon after the aggregation started. As a comparison, the

https://doi.org/10.1021/acs.langmuir.3c00787
Langmuir 2023, 39, 9744−9756

approaching speed of two solid surfaces in the experimental study of F_{cap} is controlled by the moving speed (~2 μm/s) of an AFM probe tip,[17] which is about 6 orders of magnitude lower than that observed in our modeling system. Because of the very low approaching speed in experiment, the NB bridge was assumed to be in quasi-equilibrium with the surrounding liquid. Hence, the Laplace pressure, i.e., eq 6, was directly used in the analysis of experimental data.[17] Because the approaching speed is much higher in our model system as a result of the unconstrained solid surfaces, the NB bridge is not in equilibrium with the surrounding liquid, and the ideal gas equation (eq 4) should replace the Laplace pressure in the capillary force model to calculate F_{cap}.

The presence of drag force during aggregation prevents us from directly calculating F_{cap} vs time from the cumulative force on Ag atoms in MD simulations. To find F_{cap} vs time in the MD simulation, F_{cap} is calculated for each snapshot by extracting the geometric information using the density mapping method described in Section 3.3.2. Consistent with the theoretical prediction in Figure 4, Figure 5a shows that the magnitude of F_{cap} gradually reduces as h decreases with time. After the initial 30 ns or after h drops below 15 nm, the magnitude of F_{cap} decreases faster toward zero, and the approaching speed reduces accordingly. Figure 5a shows that it took about 80 ns for the approaching speed to drop to zero. By t = 80 ns, the equilibrium separation is reached, the NB bridge is in equilibrium with the surrounding liquid, and F_{cap} approaches zero as expected. The MD simulation shows the equilibrium separation h_f = 9.4 ± 0.2 nm, which agrees well with the theoretical prediction h_f = 9.6 nm. From the MD simulation, we also found that the number of gas atoms N_g and contact angle θ (see inset of Figure 5a) were almost constant during the aggregation process. This validates the constant N_g and θ assumptions made in the improved capillary force model in Section 2.2. Furthermore, using the number of gas atoms N_g and the volume of the gas bridge at the equilibrium separation, we evaluate the density of Ne gas in the NB bridge and carry out a separation equilibrium MD simulation of a bulk Ne gas at the same density and T = 85 K. From the equilibrium MD simulation, we find the pressure of the bulk Ne gas and evaluate the compressibility factor of the gas to be ~0.95, which indicates that the ideal gas approximation for the gas inside the NB bridge in the improved capillary force model is also valid. Hence, it is reasonable to see that the improved capillary force model gives an accurate prediction of the equilibrium separation.

4.1.2. Dependence of the NBIA Dynamics on the Initial State of the NB Bridge. In this section, we keep the surface wettability at θ = 80° (c = 0.60) and study effects of the initial state of the NB bridge on the NBIA dynamics. In simulation case #2, we set the initial separation h_0 between two Ag plates to 5 nm and directly generate an NB bridge with the same number of gas atoms N_g, contact angle θ, and temperature T as those in case #1. As discussed in Section 2.2, the equilibrium separation h_f between two parallel smooth surfaces only depends on three parameters: N_g, θ, and T. Accordingly, h_f for simulation case #2 should also be close to 9.6 nm. Because h_0 = 5 nm is below h_f, the improved capillary force model predicts that F_{cap} acting on the two plates will be repulsive as shown in Figure 4. Under the repulsive F_{cap}, the MD simulation shows that the two Ag surfaces depart from each other until the equilibrium separation is reached after 3 ns. In spite of the difference in the initial state of the NB bridge, our MD simulations show that the equilibrium separation in case #2 is the same as that in case #1 as expected.

We further study the effects of the initial size of surface NBs on the NBIA dynamics. In case #3, we reduce the diameter of surface NBs from 25 to 20 nm. Because of the smaller NB size, the total number of gas atoms N_g inside the NB bridge and the initial separation h_0 at which the NBIA begins both reduce as shown in Table 2. The capillary force model predicts that smaller N_g and h_0 of a convex NB bridge will result in a smaller magnitude of attractive F_{cap} at the initial stage of the aggregation. Therefore, it is reasonable to see in Figure 5b that the initial approaching speed of the two plates with smaller initial surface NBs is lower than that in Figure 5a, which has larger initial surface NBs. Figure 5b shows that the NBIA process of case #3 was completed in ~80 ns and the equilibrium separation was also reached when the attractive F_{cap} reduced to zero as expected.

In simulation case #4, we set the initial diameter of surface NBs to 25 and 15 nm, respectively. Although the initial size of NBs on the two surfaces is different, it is seen in Figure 5c that the coalescence of the two surface NBs resulted in a convex NB bridge that has the same contact radius on the two Ag surfaces. Therefore, it is reasonable to see in Figure 5a–c that the three simulation cases (case #1, #3, and #4) that involve convex NB bridges all have similar NBIA dynamics. For an NBIA process induced by a convex NB bridge, our improved capillary force model predicts that the final equilibrium separation h_f is only determined by N_g, θ, and T. The theoretical predictions of h_f for the first four simulation cases are all verified by the MD simulation results summarized in Table 2.

4.2. NBIA of Smooth Hydrophobic Surfaces. To study the NBIA of smooth hydrophobic surfaces, we set c = 0.50 for Ar–Ag interactions, which results in a liquid-side contact angle $\theta \approx 102°$. In Figure 5d–f, the initial diameters of NBs on hydrophobic surfaces are the same as those on hydrophilic surfaces in Figure 5a–c, respectively. Upon coalescence of NBs on two hydrophobic surfaces, a concave NB bridge is formed, which results in an attractive NBCF. The capillary force model predicts that F_{cap} induced by a concave NB bridge will remain attractive during the aggregation process and its magnitude will increase as the two solid surfaces approach each other.[14] As shown in Figure 5d–f, F_{cap} found in MD simulations is consistent with the theoretical prediction. Because the magnitude of F_{cap} in the model concave bridge cases is considerably greater than that in the model convex bridge cases, the concave simulations took much less time than convex simulations to fully aggregate as shown in Figure 5.

As the magnitude of F_{cap} increases, the MD simulation results show that the two solid plates accelerate toward each other until the NB bridge expands to the edge of the solid plates where the pinning of the contact line occurs. t_{pin} is the moment when the contact line of the NB bridge is pinned at the edge of plates. After t_{pin}, the further approach of the two plates will squeeze the gas inside the NB bridge and increase gas pressure, which will in turn reduce the approaching speed of the plates and cause the NB bridge to inflate. It is seen in the insets of Figure 5d–f that the contact angle is almost a constant before t_{pin} but starts to decrease from ~102° to below 90° after t_{pin}. It is not easy to accurately measure the variation of contact angles after t_{pin} because two solid plates are very close (a few nanometers) to each other. To give a better estimate of the variation of contact angle after t_{pin}, as shown in

https://doi.org/10.1021/acs.langmuir.3c00787
Langmuir 2023, 39, 9744–9756

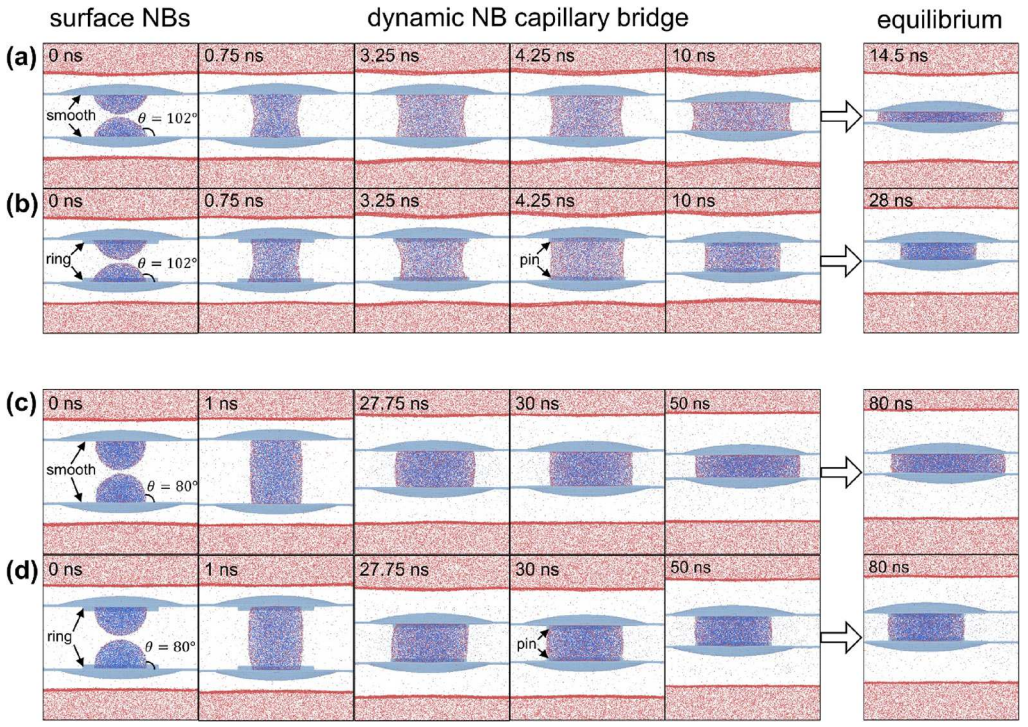

Figure 6. Snapshots showing aggregation progression of concave (a, b) and convex (c, d) NB bridges on smooth and rough surfaces.

the insets of Figure 5d–f, we first obtained the averaged contact angles (θ_{avg}) before t_{pin} and then fitted the contact angles after t_{pin} with a third-order polynomial with the left boundary fixed at θ_{avg} and the right boundary's derivative set to zero. The fitted curve of θ vs t is used in the capillary force model to determine F_{cap}.

The nearly constant contact angle θ before t_{pin} indicates that contact angle hysteresis has negligible effects on the model NBIA dynamics. As θ decreases after t_{pin}, the geometry of the NB bridge changes from concave to convex and the gas pressure in the NB bridge increases. Eventually, the repulsive pressure force balances the attractive surface tension force, which makes $F_{cap} = 0$. It is seen in Figure 5d–f that within 2 ns after t_{pin}, the attractive F_{cap} and the approaching speed of plates quickly reduce to zero. Consequently, the separation distance and the NB bridge between two hydrophobic plates become stable. Table 3 summarizes the simulation parameters for the three cases (case #5, #6, and #7) of NBIA of hydrophobic surfaces and the final equilibrium separation obtained from the MD simulation for each case. The above analysis shows that the contact line pinning plays a critical role in NBIA of the model hydrophobic surfaces.

4.3. NBIA of Rough Surfaces. To study NBIA of rough surfaces, we added a 2 nm thick solid Ag ring to each of the inside surfaces of Ag plates as depicted in Figure 1e and ran two more simulations, i.e., case #8 with a rough hydrophilic surface and case #9 with a rough hydrophobic surface. As shown in Table 4, the simulation case #8 and case #9 have the same initial simulation parameters as those in case #1 and case #5, respectively, except with a rough surface. Because the inner radius of the ring bulge on Ag surfaces is greater than the initial contact radius of surface NBs, the coalescence of surface NBs and the initial stage of the NBIA process are not affected by the ring bulge. Once the NB bridge expands to the ring bulge during the NBIA process, however, the MD simulation results show the contact line pinning will occur, and the subsequent aggregation process will be different from that on smooth surfaces.

Figure 6 visually highlights the similarities and differences between smooth and rough surfaces for convex and concave NB bridges by comparing the MD simulation snapshots. The front half of the ring bulge is hidden to clearly show the NB bridge near the solid surface. Before the contact lines reach the ring bulge, the aggregation process of the model rough surfaces is almost identical to that on the corresponding smooth surfaces. Whereas the NB bridges on smooth surfaces continue to expand until it reaches the equilibrium separation (hydrophilic case) or reaches the edge of the plates (hydrophobic case), the pinning of contact lines at the ring bulge prevents further expansion of NB bridges along rough surfaces. Similar to the effects of contact line pinning at the edge of hydrophobic plates in Section 4.2, the pinning of contact lines at the ring bulge of rough surfaces also leads to compression of the NB bridge in the aggregation process after t_{pin}. The increased gas pressure inside the NB bridge gradually reduces F_{cap} to zero and inflates the NB bridge, which causes a reduction of the contact angle as shown in Figure 7. After F_{cap} approaches zero, the separation between two rough plates begins to plateau as expected. Because of the pinning effect at the ring bulge, the aggregating rough surfaces finally reach equilibrium at larger separation as compared to corresponding smooth surfaces as shown in Figure 6 and Table 4.

4.4. Detachment of the NB Bridge from Hydrophilic Surfaces. *4.4.1. Bridge Detachment Observed in MD Simulations.* Our MD simulation results show that the coalescence of surface NBs could result in the aggregation of both hydrophilic and hydrophobic surfaces. But the aggregation of hydrophilic surfaces is slower than their hydrophobic counterparts because the convex NB bridge between hydrophilic surfaces produces a smaller F_{cap} than the similar-sized concave NB bridge between hydrophobic surfaces as shown in Figure 5. This raises a question of whether there is

https://doi.org/10.1021/acs.langmuir.3c00787
Langmuir 2023, 39, 9744−9756

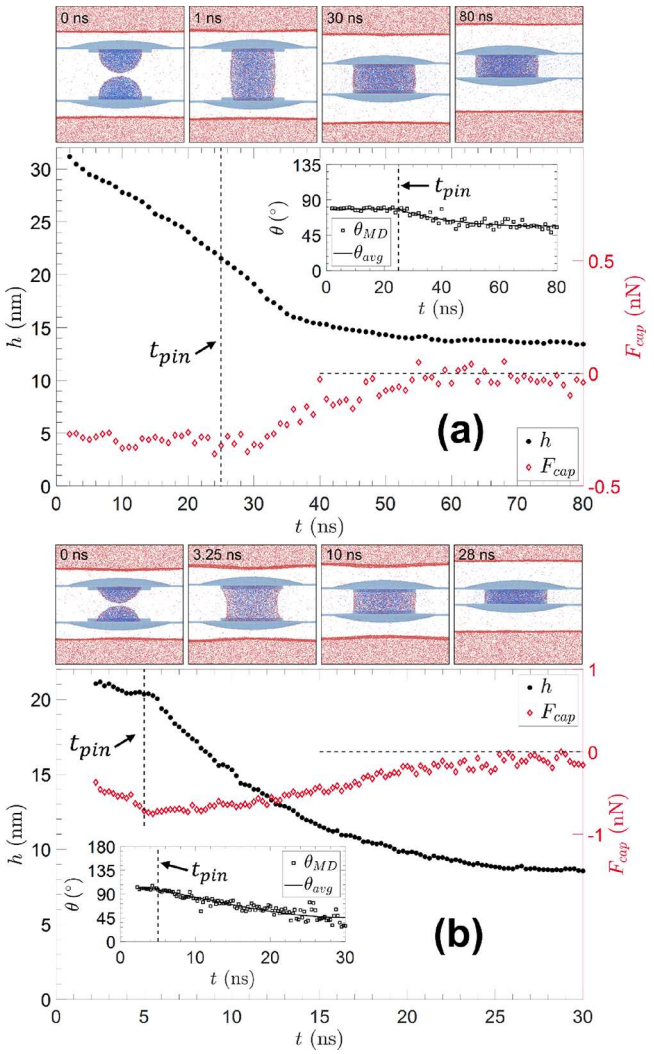

Figure 7. Separation distance, capillary force, contact angles, and snapshots over time for aggregation of two (a) rough hydrophilic surfaces and (b) rough hydrophobic surfaces.

a critical contact angle below which the coalescence of surface NBs will not result in particle aggregations anymore. To answer this question, we gradually increase the c value for Ag–Ar interactions, which makes the model Ag surfaces more hydrophilic than those in Section 4.1, and carry out MD simulations to see when the NB coalescence fails to cause aggregation of model surfaces.

The initial diameter of surface NBs is 20 nm for all cases in this section. As shown in Figure 8a, when the contact angle is reduced to ∼58° (c = 0.67), the NB bridge structure can still be well preserved after coalescence, and the NBIA process is very similar to those of hydrophilic surfaces in Section 4.1. However, when the contact angle is further reduced to ∼42° (c = 0.71), we observed that the NB bridge detached from solid surfaces soon after the coalescence of surface NBs as shown in Figure 8b. In this case, the two solid surfaces will not aggregate. To determine the *a priori* contact angle at which detachment of the NB bridge in the model system will occur, we carry out thermodynamic analysis of the detachment process in Section 4.4.2. Establishing a detachment criterion can help determine if the two solid surfaces will aggregate or not.

4.4.2. Thermodynamic Analysis of Bridge Detachment. To conduct the thermodynamic analysis, we start by

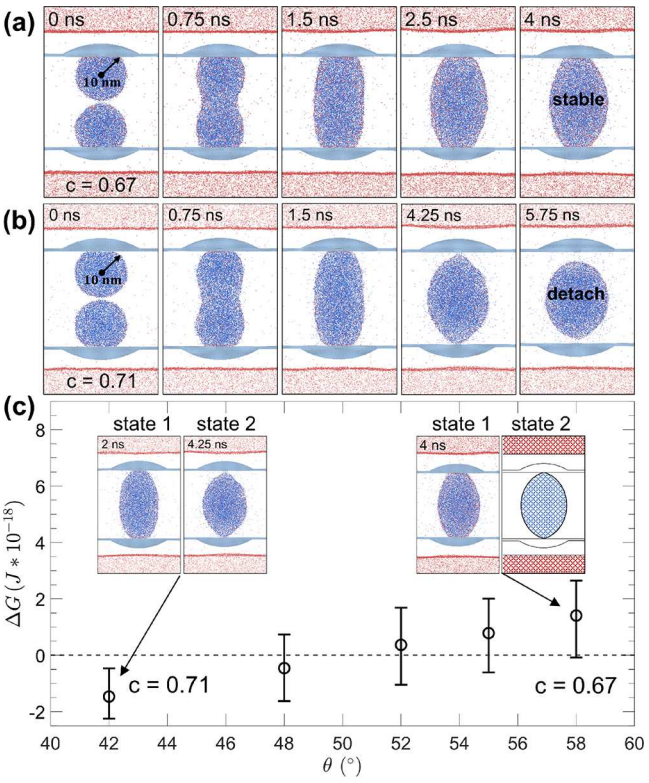

Figure 8. Snapshots of hydrophilic NB bridges in (a) stable and (b) detached configurations and (c) the difference in Gibbs free energy between states 1 and 2 for five NB bridges with different initial contact angles (θ ranges from 58 to 42°). The uncertainty of ΔG is estimated based on the uncertainties in the measurement of geometric parameters at state 1 and the error propagation in eq 18.

considering two states as shown in Figure 8c. State 1 is the moment when a fully developed NB bridge is formed after the coalescence of two surface NBs. At state 1, the gas inside the NB bridge is enclosed by two solid–gas interfaces with a total interface area of $2\pi r_0^2$ and a liquid–gas interface with an area of A_1. Accordingly, the Gibbs free energy of the NB bridge at state 1 is

$$G_1 = H_1 - TS_1 + \gamma_{sg} 2\pi r_0^2 + \gamma A_1, \tag{15}$$

where H_1 and S_1 are, respectively, the enthalpy and entropy of gas in the NB bridge at state 1 and γ_{sg} and γ are, respectively, the solid–gas surface tension and liquid–gas surface tension. State 2 is the moment when the contact radius of the NB bridge on solid surface reduces to zero (r_0 = 0), i.e., the detachment of the NB bridge is about to occur. At state 2, the solid–gas interfaces in state 1 are replaced by solid–liquid interfaces, and the area of liquid–gas interface is changed to A_2. Accordingly, the Gibbs free energy at state 2 is given by

$$G_2 = H_2 - TS_2 + \gamma_{sl} 2\pi r_0^2 + \gamma A_2, \tag{16}$$

where H_2 and S_2 are, respectively, the enthalpy and entropy of gas in the NB bridge at state 2 and γ_{sl} is the solid–liquid surface tension. Assuming ideal gas in the bridge and an isothermal detachment process, we have $H_1 = H_2$. Then, the Gibbs free energy difference between two states is

$$\Delta G = -T(S_2 - S_1) + (\gamma_{sl} - \gamma_{sg}) 2\pi r_0^2 + \gamma(A_2 - A_1), \tag{17}$$

https://doi.org/10.1021/acs.langmuir.3c00787
Langmuir 2023, 39, 9744–9756

Substituting the entropy-change relation for ideal gases in an isothermal process[39] and the Young equation[40] that defines the relationship between the contact angle and surface tensions into eq 17, we obtain

$$\Delta G = -N_g k_B T \ln(V_2/V_1) + \gamma(A_2 - A_1 - 2\pi r_0^2 \cos\theta), \quad (18)$$

where V_1 and V_2 are the volume of NB bridge at state 1 and state 2, respectively.

At state 1, all geometric parameters (r_0, r_1, r_2, h, and θ) and number of gas molecules (N_g) are obtained by direct inspection of the snapshot. To evaluate ΔG, we assume that the number of gas molecules (N_g), temperature (T), and separation (h) between two solid plates remain the same from state 1 to state 2 and set $r_0 = 0$ at state 2. Accordingly, only the principal radii (r_1 and r_2) and the contact angle (θ) will change between the two states. With $r_0 = 0$, we use eqs 7 through 9 to find the three geometric parameters (r_1, r_2, and θ) at state 2. Substituting all the geometric parameters into eqs 4 and 5, we find V and A of the NB bridge at state 1 and state 2 and evaluate ΔG from eq 18. At the critical contact angle, $\Delta G \approx 0$. Below the critical contact angle, $\Delta G < 0$, and the detachment of the NB bridge from solid surfaces will occur.

To find the critical contact angle, we carried out five MD simulations with contact angles ranging from 58 to 42° (c values vary from 0.67 to 0.71) and observed the detachment of the NB bridge in three cases with the contact angle $\theta \leq 52°$. For the model system described in this section, therefore, the critical contact angle is ~52°. To compare the modeling results with the prediction from the thermodynamic model, we evaluate ΔG of each of the five modeling cases using the aforementioned thermodynamic analysis. As shown in Figure 8c, we find that the two cases ($\theta < 52°$) with detached NB bridges have a negative ΔG, and the NB bridges in the two cases with $\theta > 52°$ are stable and their ΔG's are positive. In the case when $\theta \approx 52°$, the ΔG is close to zero and the detachment of the NB bridge occurs. The MD simulation results indicate that eq 18 gives a good prediction of the critical contact angle where NB bridge detachment occurs.

5. CONCLUSIONS

Using MD simulations, we studied the nanobubble-induced aggregation (NBIA) of two parallel plates in liquids. The following conclusions are drawn from our modeling results:

The coalescence of NBs on two adjoining surfaces could result in the aggregation of both hydrophobic surfaces and hydrophilic surfaces.

For two smooth hydrophilic surfaces, the fully aggregated surfaces were found adhered to each other by a convex NB bridge. The equilibrium separation between two smooth hydrophilic surfaces in a given liquid is only determined by the number of gas molecules in the NB bridge, the contact angle, and the temperature and can be accurately predicted by the improved capillary force model.

Contact line pinning plays a critical role in NBIA of smooth hydrophobic surfaces. When the concave NB bridge expands to the edge of hydrophobic surfaces, the pinning of the contact line at the edge reduces the contact angle, which results in a variation of bridge geometry from concave to convex. Eventually, the two smooth hydrophobic surfaces also adhere to each other by a convex NB bridge.

The pinning of the contact line could also occur at the bulge of rough surfaces. As the bulge on solid surfaces prevents further expansion of the NB bridge along the surface, the equilibrium separation between rough surfaces was found to be larger than that for corresponding smooth surfaces.

Our thermodynamic analysis of the NBIA process predicts that there is a critical contact angle below which the coalescence of surface NBs will result in the detachment of the NB bridge instead of the aggregation of surfaces. The theoretical prediction is corroborated by MD simulation results.

■ ASSOCIATED CONTENT

Data Availability Statement

The data that support the findings of this study are available from the corresponding author upon reasonable request.

■ AUTHOR INFORMATION

Corresponding Author

Zhi Liang − *Department of Mechanical and Aerospace Engineering, Missouri University of Science and Technology, Rolla, Missouri 65409, United States*; Email: zlch5@mst.edu

Author

Eric Bird − *Department of Mechanical and Aerospace Engineering, Missouri University of Science and Technology, Rolla, Missouri 65409, United States*; orcid.org/0009-0002-3051-577X

Complete contact information is available at: https://pubs.acs.org/10.1021/acs.langmuir.3c00787

Notes

The authors declare no competing financial interest.

■ ACKNOWLEDGMENTS

This work was supported by NSF under Grant No. 2310901. Additionally, we would like to thank the eXtreme Science and Engineering Discovery Environment (XSEDE) for providing us supercomputer resources for MD simulations.

■ REFERENCES

(1) Alheshibri, M.; Qian, J.; Jehannin, M.; Craig, V. S. J. A History of Nanobubbles. *Langmuir* **2016**, *32*, 11086−11100.

(2) Ahmadi, R.; Khodadadi, D. A.; Abdollahy, M.; Fan, M. Nano-Microbubble Flotation of Fine and Ultrafine Chalcopyrite Particles. *Int. J. Min. Sci. Technol.* **2014**, *24*, 559−566.

(3) Calgaroto, S.; Azevedo, A.; Rubio, J. Flotation of Quartz Particles Assisted by Nanobubbles. *Int. J. Miner. Process.* **2015**, *137*, 64−70.

(4) Zhou, W.; Chen, H.; Ou, L.; Shi, Q. Aggregation of Ultra-Fine Scheelite Particles Induced by Hydrodynamic Cavitation. *Int. J. Miner. Process.* **2016**, *157*, 236−240.

(5) Li, H.; Hu, L.; Song, D.; Lin, F. Characteristics of Micro-Nano Bubbles and Potential Application in Groundwater Bioremediation. *Water Environ. Res.* **2014**, *86*, 844−851.

(6) Agarwal, A.; Ng, W. J.; Liu, Y. Principle and Applications of Microbubble and Nanobubble Technology for Water Treatment. *Chemosphere* **2011**, *84*, 1175−1180.

(7) Wu, Z.; Chen, H.; Dong, Y.; Mao, H.; Sun, J.; Chen, S.; Craig, V. S. J.; Hu, J. Cleaning Using Nanobubbles: Defouling by Electrochemical Generation of Bubbles. *J. Colloid Interface Sci.* **2008**, *328*, 10−14.

(8) Chan, C. U.; Ohl, C. D. Total-Internal-Reflection-Fluorescence Microscopy for the Study of Nanobubble Dynamics. *Phys. Rev. Lett.* **2012**, *109*, No. 174501.

(9) Ma, T.; Kimura, Y.; Yamamoto, H.; Feng, X.; Hirano-Iwata, A.; Niwano, M. Characterization of Bulk Nanobubbles Formed by Using a Porous Alumina Film with Ordered Nanopores. *J. Phys. Chem. B* **2020**, *124*, 5067−5072.
(10) Ishida, N.; Inoue, T.; Miyahara, M.; Higashitani, K. Nano Bubbles on a Hydrophobic Surface in Water Observed by Tapping-Mode Atomic Force Microscopy. *Langmuir* **2000**, *16*, 6377−6380.
(11) Guo, Z.; Liu, Y.; Xiao, Q.; Schönherr, H.; Zhang, X. Modeling the Interaction between AFM Tips and Pinned Surface Nanobubbles. *Langmuir* **2016**, *32*, 751−758.
(12) Shin, D.; Park, J. B.; Kim, Y.-J.; Kim, S. J.; Kang, J. H.; Lee, B.; Cho, S.-P.; Hong, B. H.; Novoselov, K. S. Growth Dynamics and Gas Transport Mechanism of Nanobubbles in Graphene Liquid Cells. *Nat. Commun.* **2015**, *6*, 6068.
(13) Switkes, M.; Ruberti, J. W. Rapid Cryofixation/Freeze Fracture for the Study of Nanobubbles at Solid-Liquid Interfaces. *Appl. Phys. Lett.* **2004**, *84*, 4759−4761.
(14) Bird, E.; Liang, Z. Nanobubble Capillary Force between Parallel Plates. *Phys. Fluids* **2022**, *34*, No. 013301.
(15) Attard, P. Thermodynamic Analysis of Bridging Bubbles and a Quantitative Comparison with the Measured Hydrophobic Attraction. *Langmuir* **2000**, *16*, 4455−4466.
(16) Andrienko, D.; Patrício, P.; Vinogradova, O. I. Capillary Bridging and Long-Range Attractive Forces in a Mean-Field Approach. *J. Chem. Phys.* **2004**, *121*, 4414−4423.
(17) Hampton, M. A.; Nguyen, A. V. Systematically Altering the Hydrophobic Nanobubble Bridging Capillary Force from Attractive to Repulsive. *J. Colloid Interface Sci.* **2009**, *333*, 800−806.
(18) Hampton, M. A.; Donose, B. C.; Nguyen, A. V. Effect of Alcohol-Water Exchange and Surface Scanning on Nanobubbles and the Attraction between Hydrophobic Surfaces. *J. Colloid Interface Sci.* **2008**, *325*, 267−274.
(19) Zhang, F.; Gui, X.; Xing, Y.; Cao, Y.; Che, T. Study of Interactions between Interfacial Nanobubbles and Probes of Different Hydrophobicities. *ACS Omega* **2020**, *5*, 20363−20372.
(20) Liang, Z.; Chandra, A.; Bird, E.; Keblinski, P. A Molecular Dynamics Study of Transient Evaporation and Condensation. *Int. J. Heat Mass Transfer* **2020**, *149*, No. 119152.
(21) Liang, Z.; Keblinski, P. Molecular Simulation of Steady-State Evaporation and Condensation in the Presence of a Non-Condensable Gas. *J. Chem. Phys.* **2018**, *148*, No. 064708.
(22) Chandra, A.; Keblinski, P. Investigating the Validity of Schrage Relationships for Water Using Molecular Dynamics Simulations. *J. Chem. Phys.* **2020**, *153*, No. 124505.
(23) Gonzalez, J.; Ortega, J.; Liang, Z. Prediction of Thermal Conductance at Liquid-Gas Interfaces Using Molecular Dynamics Simulations. *Int. J. Heat Mass Transfer* **2018**, *126*, 1183−1192.
(24) Bird, E.; Liang, Z. Transport Phenomena in the Knudsen Layer near an Evaporating Surface. *Phys. Rev. E* **2019**, *100*, No. 043108.
(25) Bird, E.; Zhou, J.; Liang, Z. Coalescence Speed of Two Equal-Sized Nanobubbles. *Phys. Fluids* **2020**, *32*, 123304.
(26) Bird, E.; Smith, E.; Liang, Z. Coalescence Characteristics of Bulk Nanobubbles in Water: A Molecular Dynamics Study Coupled with Theoretical Analysis. *Phys. Rev. Fluids* **2021**, *6*, No. 093604.
(27) Foiles, S. M.; Baskes, M. I.; Daw, M. S. Embedded-Atom-Method Functions for the Fcc Metals Cu, Ag, Au, Ni, Pd, Pt, and Their Alloys. *Phys. Rev. B* **1986**, *33*, 7983−7991.
(28) Hampton, M. A.; Nguyen, A. V. Nanobubbles and the Nanobubble Bridging Capillary Force. *Adv. Colloid Interface Sci.* **2010**, *154*, 30−55.
(29) Weijs, J. H.; Snoeijer, J. H.; Lohse, D. Formation of Surface Nanobubbles and the Universality of Their Contact Angles: A Molecular Dynamics Approach. *Phys. Rev. Lett.* **2012**, *108*, No. 104501.
(30) Scott, R.; Allen, M. P.; Tildesley, D. J. Computer Simulation of Liquids. *Math. Comput.* **1991**, *57*, 442.
(31) Rappe, A. K.; Casewit, C. J.; Colwell, K. S.; Goddard, W. A., III; Skiff, W. M. UFF, a Full Periodic Table Force Field for Molecular Mechanics and Molecular Dynamics Simulations. *J. Am. Chem. Soc.* **1992**, *114*, 10024−10035.
(32) Verlet, L. Computer "Experiments" on Classical Fluids. I. Thermodynamical Properties of Lennard-Jones Molecules. *Phys. Rev.* **1967**, *159*, 98.
(33) Plimpton, S. Fast Parallel Algorithms for Short-Range Molecular Dynamics. *J. Comput. Phys.* **1995**, *117*, 1−19.
(34) Evans, D. J.; Holian, B. L. The Nose-Hoover Thermostat. *J. Chem. Phys.* **1985**, *83*, 4069−4074.
(35) Ducker, W. A. Contact Angle and Stability of Interfacial Nanobubbles. *Langmuir* **2009**, *25*, 8907−8910.
(36) Stukowski, A. Visualization and Analysis of Atomistic Simulation Data with OVITO-the Open Visualization Tool. *Modell. Simul. Mater. Sci. Eng.* **2010**, *18*, No. 015012.
(37) Scocchi, G.; Sergi, D.; D'Angelo, C.; Ortona, A. Wetting and Contact-Line Effects for Spherical and Cylindrical Droplets on Graphene Layers: A Comparative Molecular-Dynamics Investigation. *Phys. Rev. E* **2011**, *84*, No. 061602.
(38) Weijs, J. H.; Marchand, A.; Andreotti, B.; Lohse, D.; Snoeijer, J. H. Origin of Line Tension for a Lennard-Jones Nanodroplet. *Phys. Fluids* **2011**, *23*, No. 022001.
(39) Cengel, Y. A.; Boles, M. A.; Kanoglu, M. *Thermodynamics: An Engineering Approach*; McGraw-hill: New York, 2011; Vol. *5*.
(40) Young, T. An Essay on the Cohesion of Fluids. *Abstr. Pap. Printed Philos. Trans. R. Soc. London* **1832**, *1*, 171−172.

https://doi.org/10.1021/acs.langmuir.3c00787
Langmuir 2023, 39, 9744−9756